RSC Advances

PAPER

View Article Online
View Journal | View Issue

Cite this: *RSC Adv.*, 2014, **4**, 63110

Efficient removal of a typical dye and Cr(VI) reduction using N-doped magnetic porous carbon†

Shouwei Zhang,[ab] Xiangxue Wang,[b] Jiaxing Li,*[b] Tao Wen,[b] Jinzhang Xu*[a] and Xiangke Wang*[bc]

Received 11th September 2014
Accepted 3rd November 2014

DOI: 10.1039/c4ra10189h

www.rsc.org/advances

N-doped magnetic porous carbon (N-MPC) was prepared by a simple, one-step simultaneous activation-graphitization and activation route. The as-prepared N-MPC had an interconnected hierarchical structure and magnetic properties, with an ultrahigh surface area of ~2148.42 m^2 g^{-1} and a high pore volume of ~1.26 cm^3 g^{-1}. The N-MPC composites had excellent dye removal capacities (1284.09 mg g^{-1} for methylene blue, 819.39 mg g^{-1} for rhodamin B, 376.29 mg g^{-1} for victoria blue and 565.41 mg g^{-1} for methyl orange) and also had a high reducing ability for Cr(VI). These properties were attributed to the low isoelectric point, high surface area, the aggregation of dyes on N-MPC surface and the metallic Ni(0) embedded in the unique structure. Moreover, the magnetic separation also facilitated its application in wastewater treatment on a large scale. Our results showed that the N-MPC composites have a superb removal capability of Cr(VI) and dyes from water, with important potential practical applications for wastewater clean-up. In addition, the ultrahigh surface area and large pore volume of N-MPC has great potential in many future applications, such as lithium ion batteries, supercapacitors and in photocatalysis.

1 Introduction

With the development of society and economy, the increasing number of pollutants reaching the wastewater or drinking water systems, such as heavy metal ions and dyes, have become an urgent problem to the ecosystem due to their high toxicity and visibility.[1–3] Therefore, scientists have dedicated significant efforts for developing effective techniques to remove heavy metal ions and dyes from the large volumes of aqueous solutions, such as ozone treatment, chemical precipitation, ion exchange, physical/chemical adsorption, and filtration.[4–7] Among these methods, adsorption technology is one of the most important, economical and easily regenerated processes, which could effectively remove heavy metal ions and dyes without producing any by-products, thus avoiding secondary pollution.[8–12] Nevertheless, the common adsorbents, such as clay minerals, biosorbents, and metal oxides, often show limited adsorption efficiency and low adsorption capacities due to their hydrophobicity and weak affinity with heavy metal ions and dyes. In recent years, carbon materials, such as active carbon (AC) and carbon nanotubes (CNTs), have been proposed as effective advanced adsorbents to eliminate heavy metal ions and dyes from solutions.[10,13–15]

However, these carbon adsorbents still have three main shortcomings: (1) low surface area, which would limit the adsorption capacity of materials; (2) very narrow or large pore size, which would hinder the ionic/molecular diffusion, or the adsorbates could fall off easily, leading to compromised adsorption performances; (3) weak hydrophilic properties, resulting in low affinity for the adsorption of heavy metal ions and dyes from solutions. As a new material, graphene oxide can overcome these limitations due to its abundant oxygen-containing functional groups, high surface area and hydrophilic property. Moreover, it has been applied in environmental pollution clean-up as a novel adsorbent for the pre-concentration and removal of heavy metal ions and dyes from aqueous solutions.[16–19]

Although graphene oxide acts as a good adsorbent, its self-aggregation property in aqueous solution hinders the ionic/molecular diffusion, leading to compromised adsorption capacities. Moreover, it is difficult to be separated from aqueous solutions after the completion of the adsorption, thus limiting its applications in wastewater treatment. Although the graphene oxide can be separated from solution using ultracentrifugation and filtration, it requires very high speeds, and the filtration methods are prone to filter blockages. In the last decade, the application of magnetic materials has received considerable attention due to their easy separation and easy operation on a large scale. The introduction of magnetic particles into graphene can effectively solve these problems,

---

[a] *School of Materials Science and Engineering, Hefei University of Technology, 230031, Hefei, P. R. China*

[b] *Key Laboratory of Novel Thin Film Solar Cells, Institute of Plasma Physics, Chinese Academy of Sciences, P.O. Box 1126, Hefei, 230031, P. R. China. E-mail: lijx@ipp.ac.cn; xkwang@ipp.ac.cn; Fax: +86-551-65591310; Tel: +86-551-65593308*

[c] *Faculty of Engineering, King Abdulaziz University, Jeddah, 21589, Saudi Arabia*

† Electronic supplementary information (ESI) available: Kinetic models (pseudo-second-order), Langmuir and Freundlich isotherm models, *etc.* See DOI: 10.1039/c4ra10189h

especially by adding magnetic functionalities to realize magnetic separation, and thus enlarging the scope of its applications.[20,21] The composites could not only remove a variety of contaminants, but also could be quickly separated by a magnetic field on a large scale. Although the separation properties of graphene can be effectively improved after the introduction of the magnetic particles, the surface area is dramatically reduced at the same time. To maximize the adsorption properties of carbon-based adsorbents, the surface area and the magnetic properties should be balanced.

A conventional synthetic procedure to fabricate magnetic materials requires several steps with a relatively low surface area (generally <900 $m^2\ g^{-1}$) and mesoporosity (generally >7 nm), rather than microporosity. Therefore, it is a great challenge to exploit a facile and scalable method to prepare versatile advanced adsorbents with a combination of high surface area, large pore volume, and strong magnetic response. Chemical activation, a general way of preparing advanced porous materials, has been applied to prepare carbon-based materials with a high surface area and porous structure.[22,23] This method can significantly increase the number of micropores to enhance the surface area and to increase the number of active sites on surface, leading to the improved performance of the adsorbents. In addition, it has been found that the magnetic particles (such as iron, cobalt, and nickel) and/or their composites could react with the carbonaceous materials to further tune the porosity, which can be expected to functionalize the magnetic source and activation agent to tailor the pore size of carbon.[24]

Herein, we report a one-step, scalable, simultaneous activation-graphitization and activation route to fabricate N-doped magnetic porous carbon (N-MPC) with a high surface area and high pore volume, using glucose as the carbon source, melamine as the nitride source, and nickel nitrate as the catalyst and magnetic source. The novel N-MPC materials were designed on the basis of the following four considerations: (1) as an abundant, non-toxic and sustainable carbon source, glucose could coordinate with metal salt *via* its hydroxyl groups and avoid the aggregation of the carbonized carbon; (2) melamine was selected as the nitrogen source due to its low-cost, commercial availability and abundant N element; (3) Ni could be expected to function as both a magnetic source and *in situ* catalyst agent in the fast pyrolysis process to generate porous structures; (4) KOH could be added into the glucose and melamine matrix and heated to form a high surface area and large pore volume. Thus, the obtained novel composites were used as adsorbents for the efficient removal of heavy metal ions and dyes from aqueous solutions. The adsorption kinetics, isotherms and the possible removal mechanism of Cr(VI) and dyes on N-MPC, as well as the magnetic separation and recovery of used N-MPC, were investigated and are discussed in detail.

2 Materials and methods

All reagents were of analytical grade and were commercially available from Sinopharm Chemical Reagent Co., Ltd (China), and they were used without further purification.

Materials preparation

The N-MPC was synthesized by an activation-graphitization and activation route, using glucose, melamine, $Ni(NO_3)_2\cdot 6H_2O$, and KOH as the carbon source, nitrogen source, activation-graphitization source, and chemical activation agent, respectively. In a typical process, glucose (4.0 g), melamine (2.0 g), KOH (3.0 g), and $Ni(NO_3)_2\cdot 6H_2O$ (0.45 g) were mixed together and ground to a homogeneous mixture. The mixture was transferred to a tube furnace and heated to 800 °C for 1 h with 5 °C min^{-1} under Ar conditions. After cooling down to room temperature, the sample was rinsed with Milli-Q water and ethanol for three cycles and finally dried at 80 °C overnight. The yield obtained was ~0.42 g per batch. In addition, two other controlled samples were also prepared under the same experimental conditions. One was the MPC, which was made by a similar route as that of N-MPC without the addition of melamine. The other one was the Ni@(glucose + melamine) + KOH sample, defined as Ni@GM + KOH, which was prepared by the two-step processes of (1) pre-carbonization, which was made by a similar route as that of the Ni@(glucose + melamine) sample and (2) chemical activation by KOH, which was made with the same process as that of the N-MPC.

Characterization

X-ray diffraction (XRD) patterns were recorded in reflection mode (Cu Kα radiation, $\lambda = 1.5418$ Å) using a Scintag XDS-2000 diffractometer. X-ray photoelectron spectroscopy (XPS) data were obtained with an ESCA Lab220i-XL electron spectrometer from VG Scientific using 300 W Al Kα radiation. The morphologies and microstructures were observed using a field emission scanning electron microscope (FE-SEM, Sirion200, FEI Corp., Holland) and transmission electron microscopy (TEM, JEM-2011, JEOL, Japan). The UV-vis spectra were recorded on a Shimadzu UV-2550 spectrophotometer equipped with a Labsphere diffuse reflectance accessory. Thermogravimetric analysis (TGA) and differential thermal gravimetry (DTG) were performed with a NETZSCH TG209 F3 instrument under air at the heating rate of 20 °C min^{-1}. The Brunauer–Emmett–Teller (BET) method was used to calculate the specific surface areas. The N_2 adsorption–desorption isotherms at 77 K were measured using an adsorption instrument (TriStarII, Micromeritics Company, USA) to evaluate their pore structures. Raman spectra were recorded using a LabRamHR. The laser excitation was provided by a regular model laser operating at 514.5 nm. Fourier transformed infrared spectroscopy (FT-IR) was carried out on a Bruker EQUINOX55 spectrometer (Nexus) in KBr pellet at room temperature.

Adsorption experiments

Metal ion removal experiment. All adsorption experiments were performed in glass vials (50 mL). For the kinetic adsorption experiments, a stock suspension of 1.0 g L^{-1} N-MPC was dispersed into 10 mg L^{-1} heavy metal solution and shaken for 24 h. Samples were withdrawn at appropriate time intervals and the supernatant was separated by centrifugation at 8500 rpm for 15 min. The concentrations of heavy metal ions were determined by atomic absorption spectrometry.

Dyes removal experiment. All adsorption experiments were performed in glass vials (50 mL) using a batch technique. For kinetics experiments, a stock suspension of 1.0 g L^{-1} N-MPC was dispersed into 20 mL of 60 mg L^{-1} methylene blue (MB), methyl orange (MO), rhodamin B (RhB) or victoria blue (VB) solution. The samples were withdrawn at appropriate time intervals and the supernatant was separated by centrifugation at 8500 rpm for 15 min. For the adsorption isotherm experiments, 1.0 g L^{-1} N-MPC suspension was added to 20 mL of dye solution with various concentrations. The solid and liquid phases were separated by centrifugation at 8500 rpm for 15 min, after the suspensions were oscillated for 24 h. The concentrations of dyes in the supernatant were determined by UV-vis absorption spectroscopy.

The amounts of heavy metal ions/dyes adsorbed on adsorbents were calculated using the following equation:

$$q_e = \frac{(C_0 - C_e)V}{m} \quad (1)$$

where C_0 and C_e represent the initial and equilibrium concentrations of heavy metal ions/dyes (mg L^{-1}), respectively; V represents the volume of solution (L) and m represents the mass of N-MPC used (g).

3 Results and discussion

Characterization of N-MPC

The XRD patterns of the as-prepared materials are shown in Fig. 1A. The diffraction peak found at the 2θ value of 26.41° is assigned to the graphite (002) plane, and the sharp peaks at 44.52° and 51.88° can be referred to the (111) and (200) planes of the cubic structure of metallic Ni (JCPDS no. 040850). No nickel carbides or nickel oxides are detected, which is consistent with the previous results.[25] It can be seen that the intensities of graphite phase become weaker and broader in the order of N-MPC > Ni@GM + KOH > MPC. Compared to the N-MPC, the (002) peak of Ni@GM + KOH is weaker in intensity and is faintly broadened, indicating that the ordered graphite structure becomes slightly disordered after strong chemical activation reactions. However, the (002) peak of MPC disappeared due to the loss of the graphitization, indicating an important effect of N doping and Ni catalyst on the crystallinity of materials.[26] These results demonstrate that the N-MPC obtained by the one-step preparation of a catalyzed glucose and melamine leads to a high degree of graphitization. The graphitic carbon has attracted great interest in water treatment for their features of the intensive interaction of the graphitic basic plane with inorganic ions and organic dyes and good chemical and thermal stability.

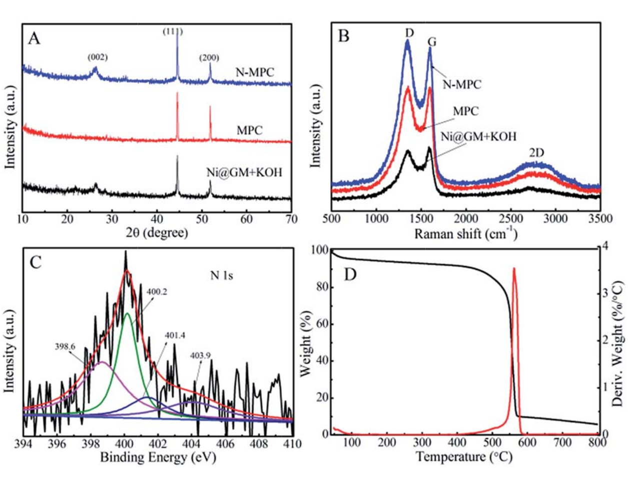

Fig. 1 The XRD patterns (A) and Raman spectra (B) of N-MPC, MPC and Ni@GM + KOH; high resolution N1s XPS spectrum of N-MPC (C), TGA and DTG curves of N-MPC (D).

Fig. 1B shows the Raman spectra of the as-prepared materials. All the materials have same peak positions of the D band (1346 cm^{-1}), corresponding to the stretching vibrations of carbon sp^2 bonds of the graphite, G band (1597 cm^{-1}), assigned to the disordered sp^2-hybridized carbon atoms of the graphite crystal, and 2D band (2700 cm^{-1}), indicating the materials contain few-layer graphene.[16,27,28] Furthermore, compared with N-MPC, the G peak of the MPC is up-shifted to 1602 cm^{-1}, which could also be seen in the CNTs and N-doped CNTs, indicating the successful fabrication of N-doped carbon materials.[26,29] The D and G bands in the Raman spectrum of Ni@GM + KOH are broader with no obvious peak of the 2D band, suggesting more disordered bonds and a much thicker layer than that in N-MPC.[23,27]

XPS was conducted to investigate the chemical composition of the materials. As expected, all the peaks assigned for carbon (C 1s), nitrogen (N 1s), nickel (Ni 2p) and oxygen (O 1s) are present in the spectra (Fig. S1A†). The high C1s spectrum resolution of N-MPC can be deconvoluted into three individual component peaks located at 284.6 ($C_{sp}{}^2$–$C_{sp}{}^2$), 285.3 (N–$C_{sp}{}^2$), and 285.9 eV (N–$C_{sp}{}^3$), confirming the successful N doping within the N-MPC material (Fig. S1B†). Similarly, the N1s spectrum of N-MPC (Fig. 1C) can be resolved into four peaks: at 398.6 eV, assigned to sp^2 N atoms connected to carbon atoms; at 400.2 eV (pyrrolic nitrogen) of trigonal N atoms connected to sp^2 or sp^3 carbon atoms; at 401.4 eV assigned to quaternary N species and at 403.9 eV, representing quaternary N-oxide species.[30,31]

TGA and DTG are employed to determine the change in the weight loss of N-MPC in air (Fig. 1D). The N-MPC is stable at low temperature, and ~89.91 wt% of weight loss occurs at 450–600 °C, which is presumably due to the oxidation of graphitic carbon. Ultimately, the carbon becomes CO_2 gas and the Ni is oxidized mainly into NiO. The results demonstrate that the content of NiO is ~5.78 wt%, corresponding to ~4.54 wt% of metallic Ni(0). The DTG result shows a peak located at ~555 °C, indicating the existence of the graphitic carbon.

The N_2 adsorption–desorption isotherms and pore size distribution of the as-prepared materials are shown in Fig. 2A and B. The N-MPC exhibits a tiny hysteresis loop in the relative pressure region of 0.4–0.9, and moderately steep adsorption curves at low relative pressure, indicating the existence of plenty of micropores in N-MPC.[32] Based on the nitrogen quantity adsorbed at different relative pressures, the N_2-BET surface area of MPC is only ~258.69 m^2 g^{-1}, and the total pore volume is ~0.18 cm^3 g^{-1}. For Ni@GM + KOH, the N_2-BET surface area is ~1051.85 m^2 g^{-1}, and the total pore volume is ~0.71 cm^3 g^{-1}. It is very interesting to note that the N_2-BET surface area of the N-MPC is ~2148.42 m^2 g^{-1}, which is 7.8 times of MPC and 1.9

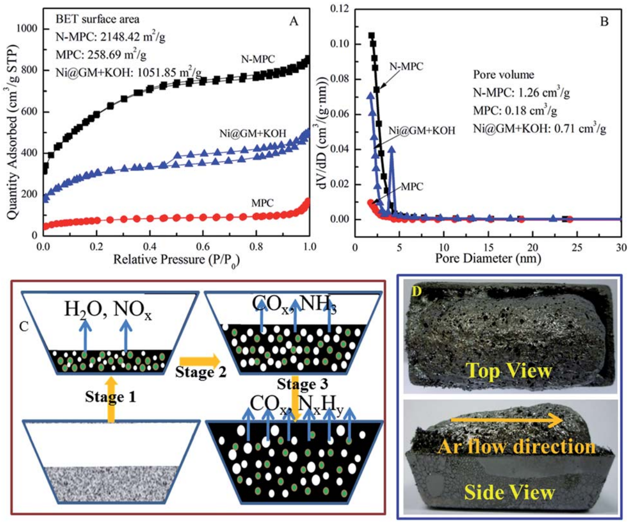

Fig. 2 Nitrogen adsorption–desorption isotherms (A) and pore-size distributions (B) of N-MPC, MPC and Ni@GM + KOH; schematic growth model for N-MPC (C), two digital images of N-MPC (Top view and Side view) (D).

times of Ni@GM + KOH. Moreover, the total pore volume is ~1.26 cm^3 g^{-1}, which is 6.7 times of MPC and 1.7 times of Ni@GM + KOH. A sharp contrast between the N-MPC and MPC can be revealed by the digital images of the two samples; the MPC occupy much less bulk volume than the N-MPC, although they have the same weight (Fig. S2†). Based on the above results, the ultrahigh BET surface area and high pore volume can be explained by the following observations (Fig. 2C): when heated to a certain temperature (*i.e.*, from ~25 to ~200 °C), NiO is formed by the thermal decomposition of nickel salt (Stage 1).[33] With further temperature increase (~200 to 500 °C), the melamine melts, inducing the polymerization of melamine, and thus forming a C–C_3N_4 polymer layer on the surface of NiO, which begins to partly decompose in the form of CO_x and NH_3 (Stage 2).[34–36] As the temperature increases (~500 to 800 °C), a large amount of gas is released with the decomposition of C_3N_4 polymer (Stage 3).[37] The as-formed bubbles expand the volume of the reaction system to ten times of its original volume and endow the final products with porosity (Fig. 2D). The porosity is further improved by KOH activation at higher temperatures.[22] NiO is reduced to metallic Ni(0), which could further catalyze the formation of graphitic frameworks, as well as further activation. The high surface area and large pore volume mean more active sites on the surface of N-MPC, which is very beneficial for the adsorption of metal ions and organic pollutants. In addition, the rational porous structure provides low-resistance and interconnected channels, resulting in the rapid diffusion of the ions/molecules within N-MPC. In addition, considering the simple synthesis procedure, the scalable synthesis of N-MPC is possible using a larger furnace.

The morphologies and structures of the as-prepared N-MPC are shown in Fig. 3. The material is stacked by very large plate-like agglomerations (Fig. 3A), which have hierarchical three-dimensional networks and consist of hundreds of plate with the thickness of ~50–150 nm (inset of Fig. 3A). Uniform metallic Ni nanoparticles are *in situ* generated during the calcination process and are well-dispersed in the framework (Fig. 3B), which are further investigated and evidenced by HRTEM images. Fig. 3C depicts a randomly selected magnified particle, which indicates a wrapped nanoparticle by a carbon layer of ~3.4 nm thickness (Fig. 3D). Moreover, the HRTEM image of the particle displays a regular lattice and the lattice distance of 0.204 nm, which is well-assigned to the (111) plane of cubic Ni (Fig. 3D); the lattice distance of 0.200 nm corresponds to the (002) plane of graphite carbon.[24] The elemental mapping of the N-MPC indicates the distribution of the three elements (O, N, and Ni) within the layer structures (Fig. 3E). It can be seen that N and Ni are homogeneously distributed in the carbon sheet.

Adsorption property of N-MPC

Removal of Cr(VI) and its removal mechanism. The removal of Cr(VI) on N-MPC after different contact times are shown in Fig. 4A. One can see that ~30 min is sufficient to achieve the adsorption equilibrium under all Cr(VI) initial concentrations, suggesting the rapid removal ability of Cr(VI) by N-MPC. In the case of an initial concentration of 6.0 mg L^{-1}, all the samples show a final removal efficiency of 100% (Fig. S3†). The rapid Cr(VI) removal can be attributed to the existence of a large number of active sites on the N-MPC surfaces. The amount of Cr(VI) adsorbed on N-MPC increases with increasing initial Cr(VI) concentrations, which can be explained by the fact that higher initial Cr(VI) concentration could provide a higher mobility driving force from the solution to the N-MPC surface, resulting in more collisions between Cr(VI) ions and the active sites on N-MPC, and thus resulting in a greater amount of Cr(VI) being adsorbed on N-MPC. The N-MPC is expected to become a

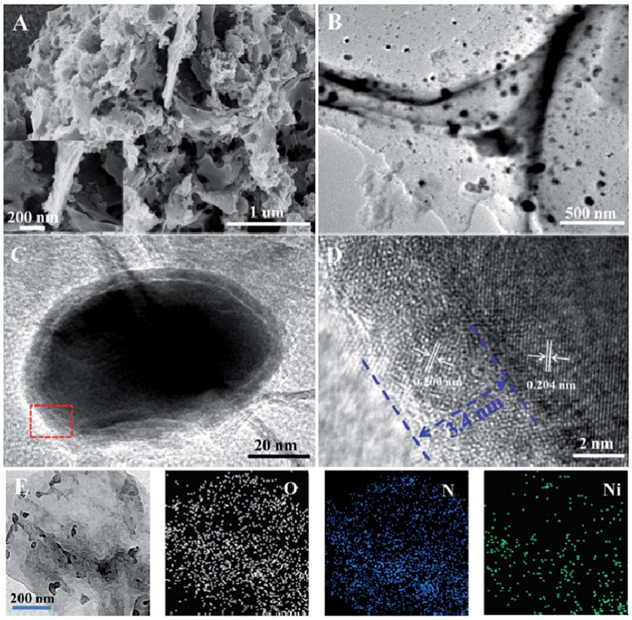

Fig. 3 Low magnification SEM image, and high magnification SEM image inset (A). TEM images with different magnifications (B–D). Elemental mapping (E) of N-MPC.

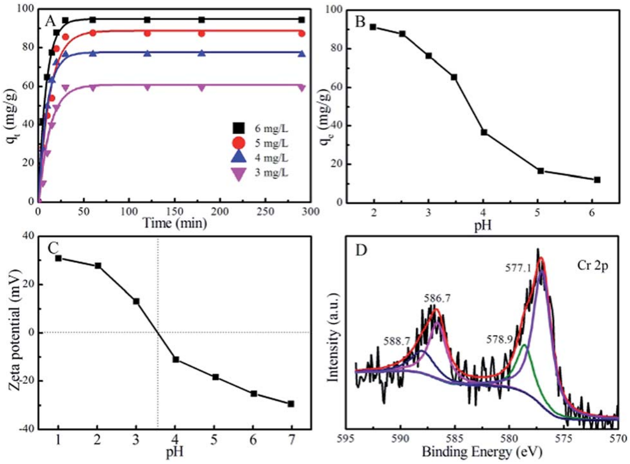

Fig. 4 Time dependent Cr(VI) adsorption on N-MPC ($C_{\text{adsorbent}} = 0.05$ g L^{-1}, $T = 25$ °C, pH ~2.5) (A), the Zeta potential (B), the pH effect ($C_{\text{adsorbent}} = 0.05$ g L^{-1}, $T = 25$ °C, $C_{\text{Cr(VI)initial}} = 6.0$ mg L^{-1}) (C) and the high resolution Cr 2p XPS spectrum after adsorption on N-MPC (D).

promising advanced material for the rapid and efficient treatment of Cr(VI)-containing wastewater because of its rapid removal rate with high removal capacity.

The kinetics of Cr(VI) adsorption on N-MPC is also simulated by the pseudo-second-order model, which describes the kinetics process as follows:

$$\frac{t}{q_t} = \frac{1}{k_2 {q_e}^2} + \frac{1}{q_e} t \tag{2}$$

where k_2 (g (mg^{-1} min^{-1})) is the pseudo-second-order rate constant, and q_e and q_t are the removal capacities at equilibrium and at contact time t (min), respectively. As can be seen from Fig. S4† and Table S1,† the experimental data are well fitted by the pseudo-second-order model. The calculated q_e values ($q_{e,cal}$) are found to be very close to the experimental q_e values ($q_{e,exp}$), which indicates that the Cr(VI) removal process on N-MPC obeys the pseudo-second-order model.

pH is one of the most important parameters affecting heavy metal ion removal.[38] At an initial Cr(VI) concentration of 6.0 mg L^{-1}, the removal percentage of Cr(VI) from solution to N-MPC decreases from ~91.3% to ~12.1% when the pH value increases from 2.0 to 6.0 (Fig. 4B), indicating an adverse pH effect in Cr(VI) removal. Depending on pH and Cr(VI) concentrations, Cr(VI) ions can exist in various anionic forms (*i.e.*, $Cr_2O_7^{2-}$, $HCrO_4^-$, CrO_4^{2-} and $HCr_2O_7^-$) in aqueous solutions (Fig. S5†). To further understand the influence of pH on Cr(VI) removal, the zeta potentials of N-MPC at different pHs are shown in Fig. 4C. The pH at point of zero charge (pH_{pzc}) of N-MPC is ~3.6, which is much lower than 6.3 (granular activated carbon), 6.2 (natural corncob), and 4.5 (untreated coffee husks).[39–41] The low pH_{pzc} is caused by the introduction of N from melamine pyrolysis.[42] Below the pH_{pzc}, the N-MPC surface is positively charged and anionic Cr(VI) adsorption occurs easily. As the pH increases, the Cr(VI) removal decreases, which is ascribed to the higher OH^- concentration competing with the anionic Cr(VI) species. On the contrary, when the N-MPC surface is negatively charged at pH > pH_{pzc}, the electrostatic repulsion between negatively charged Cr(VI) species and negatively charged N-MPC is increased, and this results in a decrease of $HCrO_4^-$ and CrO_4^{2-} adsorption. Another factor affecting this variation of removal capacity at different pH values is the adsorption free energy of various chromium species ($HCrO_4^-$ and CrO_4^{2-}) at different pH values.[43] At pH 2.0–6.0, the Cr(VI) species mainly exists as the monovalent $HCrO_4^-$, which gradually converts to a divalent CrO_4^{2-} form as the pH increases. The adsorption free energies of $HCrO_4^-$ and CrO_4^{2-} are −2.5–0.6 and −2.1–0.3 kcal mol^{-1}, respectively.[44] The adsorption free energy of $HCrO_4^-$ is lower than that of CrO_4^{2-}, and consequently $HCrO_4^-$ is more favorably adsorbed than CrO_4^{2-} at the same concentration. The removal of Cr(VI) at lower pH is mainly due to the adsorption of $HCrO_4^-$, which is expected to be adsorbed in larger quantities than CrO_4^{2-} under the same adsorption affinity.[45] Furthermore, during the experimental process, no bubbles were observed in the solution, which indicated that the carbon shell could effectively prevent the Ni cores from reacting with H^+. For instance, when the core-shell structure adsorbents were added into the solution, the carbon shells could effectively adsorb H^+ onto the shell surface and avoid direct contact between H^+ and Ni(0). The Cr(VI) was reduced to Cr(III) by metallic Ni(0), which partly oxidized to Ni(II) ions, but it could not be released into the environment to cause secondary pollution due to the presence of the carbon shells.

To further investigate the removal mechanism of Cr(VI), an XPS spectrum of N-MPC after Cr(VI) adsorption was obtained and is presented in Fig. 4D. Two peaks located at ~577.1 and 586.7 eV correspond to Cr $2p_{3/2}$ and Cr $2p_{1/2}$ asymmetric peaks, respectively. The peaks centered at ~578.9 and 588.7 eV prove the existence of the oxidation state of Cr(III).[41] These results indicate that both Cr(III) and Cr(VI) are present on the surface of N-MPC; thus, a part of the surface adsorbed Cr(VI) ions is reduced to Cr(III) by metallic Ni(0).[46] We speculated that Cr(VI) ions (more precisely $Cr_2O_7^{2-}$ ions) first get adsorbed in the porous network and get reduced to Cr(III) ions through electron transfer from the core Ni centers under the presence of H^+, and the Ni core are subsequently partly oxidized to Ni(II) ions. The Cr(III) ions thereafter remain bound in the matrix through an associated coordination with the nitrogen donors.

In conclusion, the possible removal mechanism of Cr(VI) might be explained as follows: first, the Cr(VI) anions were adsorbed on the positively charged active sites of N-MPC through electrostatic interaction. Then, the surface adsorbed Cr(VI) ions were reduced to Cr(III) by the metallic Ni(0), and then the Cr(III) ions were further captured by N-MPC.[47] N introduced into N-MPC increases the negative charge density, inducing an increase in dramatically electrostatic driving forces between the Cr(III) ions and the N-MPC, and thus N-MPC shows an extraordinary adsorption capacity and high reduction ability.

Dye removal and the removal mechanism. The removal capacities of MB, RhB, VB and MO were studied on different adsorbents (Table S2†). It can be observed from Table S2† that the q_e increases from 330.25 mg g^{-1} (activated carbon (AC)) to 1284.09 mg g^{-1} (N-MPC) for MB, from 194.32 mg g^{-1} (AC) to 819.39 mg g^{-1} (N-MPC) for RhB, from 157.52 mg g^{-1} (AC) to

376.29 mg g^{-1} (N-MPC) for VB, and from 202.76 mg g^{-1} (AC) to 565.41 mg g^{-1} (N-MPC) for MO. The adsorption capacities of the dyes on N-MPC are several times higher than those of AC. With the ultrahigh surface area and large pore volume, N-MPC exhibits the highest adsorption capacities in adsorbing the dyes. Moreover, as can be seen from Table S5,† the sorption capacity of dyes on N-MPC is higher than that of some conventional adsorbents. The above results indicate that N-MPC is a highly efficient adsorbent for the elimination of dyes from large volumes of aqueous solutions.

The adsorption isotherms of all the dyes on N-MPC are shown in Fig. 5A. The Langmuir and Freundlich models were used to describe the adsorption isotherms (SI). The corresponding parameters are given in Table 1. By comparing the regression coefficients (R^2), it was found that the adsorption behavior could be better described by the Freundlich model. Therefore, the dyes are adsorbed on the heterogeneous adsorption surface of N-MPC, suggesting that different sites with different adsorption energies are involved, and in some cases, intermolecular interactions occur between the dyes and N-MPC. The dyes have a tendency of self-aggregation in solution, *i.e.*, the dyes can form dimers (2(dye) ↔ (dye)$_2$) before further aggregation in the case of very low dye concentrations. Subsequently, the dimeric units will further aggregate (n(dye)$_2$ ↔ (dye)$_4$ + (n − 2)(dye)$_2$).[48,49] Therefore, the adsorption space may accommodate more layers of dye molecules rather than one layer of dye molecules, and not all adsorbed dye molecules are in contact with the surface of the adsorbent (N-MPC). Moreover, the porous structures of the materials may affect the adsorption behavior, resulting in the multilayer adsorption. The Brunauer–Emmett–Teller (BET) isotherm is a theoretical equation, most widely applied in gas–solid equilibrium systems. This model assumes a multilayer adsorption and was developed to describe adsorption phenomena when successive molecular layers of adsorbate form after the completion of a monolayer. The extinction of this model to a liquid-solid interface is described by eqn (3), which is linearized in eqn (4).

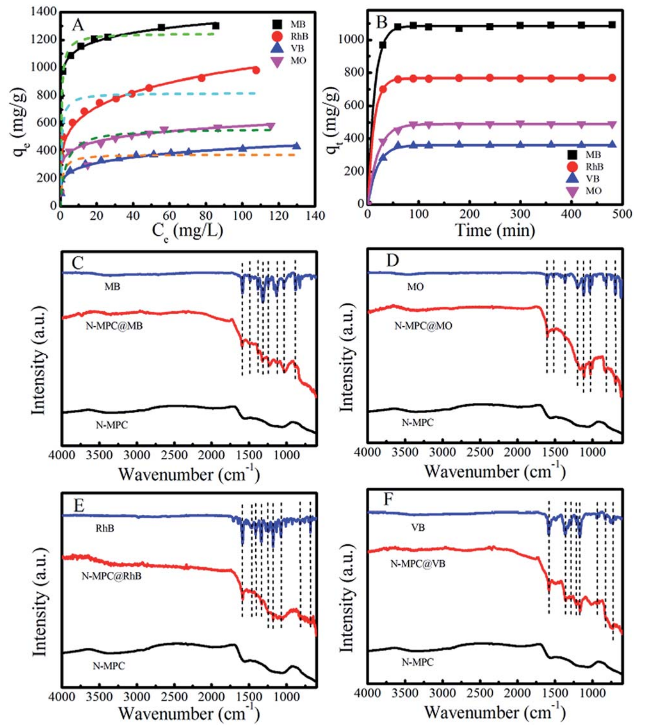

Fig. 5 The adsorption isotherms ($C_{\text{adsorbent}} = 0.05$g L^{-1}, $T = 25$ °C) (A), adsorption kinetics ($C_{\text{adsorbent}} = 0.05$ g L^{-1}, $T = 25$ °C, $C_{\text{(dye)initial}} = 60$ mg L^{-1}) (B), FTIR spectra before and after dye adsorption on N-MPC (C–F).

Table 1 The Langmuir and Freundlich isotherm model parameters of the dyes on N-MPC

		MB	RhB	VB	MO
Langmuir	q_m (mg g^{-1})	1284.09	819.39	376.29	565.41
	b (L mg^{-1})	2.14	1.76	1.02	0.35
	R^2	0.808	0.781	0.851	0.802
Freundlich	K_F	960.36	393.58	181.01	315.15
	n	0.07	0.19	0.18	0.13
	R^2	0.984	0.937	0.948	0.969

$$q_e = \frac{C_{\text{BET}} C_e q_s}{(C_s - C_e)[1 + (C_{\text{BET}} - 1)(C_e/C_s)]} \tag{3}$$

$$\frac{C_e}{(C_s - C_e)q_e} = \frac{1}{C_{\text{BET}} q_s} + \left(\frac{C_{\text{BET}} - 1}{C_{\text{BET}} q_s}\right)\left(\frac{C_e}{C_s}\right) \tag{4}$$

where q_e is the amount of adsorbate in the adsorbent at equilibrium (mg g^{-1}), C_e is the equilibrium concentration (mg L^{-1}), C_s is the adsorbate monolayer saturation concentration (mg L^{-1}), C_{BET} is the BET adsorption isotherm relating to the energy of surface interaction (L mg^{-1}) q_s is the theoretical isotherm saturation capacity (mg g^{-1}).

Considering MB and RhB as examples, from Fig. S6,† it was found that the experimental data efficiently fit the BET model isotherm, and the correlation coefficients R^2 were 0.9997 (MB) and 0.9983 (RhB), respectively. Therefore, the BET model is more suitable for describing the adsorption behavior of MB and RhB on N-MPC.

In addition, two significant differences in q_e values could be obtained from Fig. 5A and Table 1. First, an obvious difference in q_e between MB and MO, 1284.09 mg g^{-1} for MB and 565.41 mg g^{-1} for MO, could be attributed to the zeta potential of N-MPC. In our case, the N-MPC was directly added into dye-containing aqueous solutions without pH adjustment. The initial pH values of MB and MO solution were ∼5.9 and ∼4.2, respectively. The zeta potential of N-MPC was ∼−22 mV at pH of ∼5.9 (Fig. 4C), indicating the negatively charged surface of N-MPC. The strong electrostatic interaction between the negatively charged N-MPC and the positively charged MB results in the higher MB removal capacity.[50] On the contrary, the removal efficiency of MO was lower due to the electrostatic repulsion between the negatively charged N-MPC and the negatively charged MO.[50] Therefore, the different removal capacities of MB and MO on N-MPC can be attributed to their opposite charges.

Second, the difference between the adsorption capacities of MB, RhB, and VB on N-MPC are obvious, although these dyes have the same charges, which may be due to the pore structure properties and the size of dye molecules.[50] As can be seen from Table S3,† (1) MB has a short 1D chain structure and small molecular size; (2) RhB has a two-dimensional (2D) planar structure and medium molecular size; and (3) VB exhibits the largest molecular size and a three-dimensional (3D) structure. N-MPC possesses the highest removal capacity for MB due to its short 1D chain structure and small molecular size, which have a lower interaction force with the N-MPC pore wall, thus MB easily enters into N-MPC pores.[51] For RhB, when it is adsorbed in N-MPC pores, the 2D planar molecular structure has a larger adsorption resistance, inducing a lower share of the surface and a lower removal capacity.[50] VB, which has a more complex 3D structure, has the biggest adsorption resistance, resulting in the lowest removal by N-MPC.[50] Therefore, the different adsorption capacities of MB, RhB and VB on N-MPC can be attributed to the pore structure and the molecular size.

In addition, the time profiles of dye adsorption on the N-MPC are shown in Fig. 5B and Table S4.† The adsorption is nearly completed within 40 min; moreover, the N-MPC exhibits a superb adsorption capacity of 1091.31 mg g^{-1} for MB after 100 min at the initial concentration of 60 mg L^{-1}. These results indicate that N-PMC, which has a high removal capacity and high removal rate, is expected to become an excellent advanced adsorbent for the rapid and efficient treatment of dyes from the large volumes of aqueous solutions.

To further study the dye removal mechanism, FTIR was used to investigate the surface changes of N-MPC before and after dye adsorption, as shown in Fig. 5C–F. The adsorption peaks located at 3361, 1560 and 1056 cm^{-1} are attributed to the –OH, C═O and C–O, respectively. These oxygen-containing functional groups can effectively improve the hydrophilicity of N-MPC, and can also act as active sites for dye adsorption. Compared to the N-MPC, the FTIR spectrum of N-MPC@MB shows new absorption peaks at 1088 cm^{-1} (CH_3–), 1312 cm^{-1} (C–N) and 1590 cm^{-1} (C═S), indicating that MB has been adsorbed on the surface of N-MPC4. For MO, the S═O stretching vibration in MO shifts to a lower wavenumber of 1050 cm^{-1}, which indicates that MO has been anchored onto the surface of N-MPC during the removal process. For all dyes, the characterized peaks obviously decrease in intensity and significantly broaden after the treatment, indicating a slight change in the property of the dye after the adsorption on N-MPC.

The reusability of the N-MPC was also studied. From Fig. 6A, in the case of an initial concentration of 65 mg L^{-1}, the $q_{\max}$ decreases from ~1248.09 to ~1149.51 mg g^{-1} for MB, from ~819.39 to ~739.24 mg g^{-1} for RhB, from ~376.29 to ~336.59 mg g^{-1} for VB, and from ~565.41 to ~495.66 mg g^{-1} for MO, respectively. Therefore, the N-MPC still had ~92.1%, ~90.2%, ~89.4% and ~86.7% removal capacities for MB, RhB, VB and MO, respectively, after eight cycles, indicating that N-MPC has excellent reusability for bulk dye removal.

In addition to the high removal ability and reusability, Rapid separation from solution is also extremely important for practical applications. The magnetic property of N-MPC is shown in Fig. 6B, the M_s of N-MPC is ~37.83 emu g^{-1}. The digital images for MB before and after adsorption by the N-MPC are shown in Fig. 6C and Movie S1.† As can be seen, MB is completely adsorbed by N-MPC within 1 min, indicating its high adsorption rate. When a magnet is applied, the adsorbent can be rapidly separated from the solution, and the MB solution becomes clear. Once the magnet is withdrawn, the particles can be immediately re-dispersed into the solution by slight shaking. Notably, the N-MPC can immediately be used in the next cycle and 89.9% of MB can be removed even after 15 cycles. Thus, N-MPC can be applied as a potential advanced adsorbent for the treatment of certain dye polluted wastewater for environmental pollution clean-up because of its rapid separation and high adsorption properties.

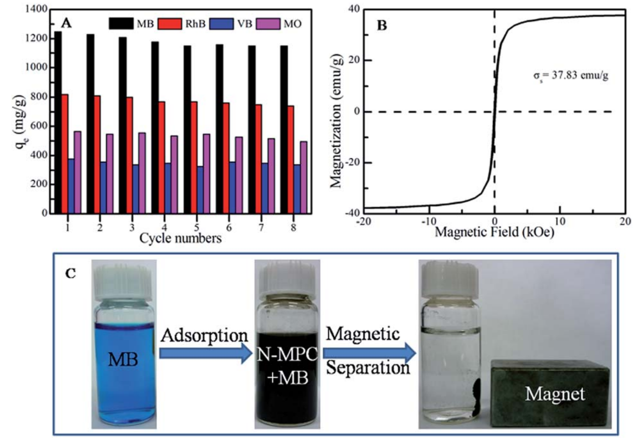

Fig. 6 The recycling performance (A), room temperature magnetization curves of N-MPC (B), and digital images showing the magnetic separation performance of N-MPC after the adsorption of MB (C).

4 Conclusions

In the present study, N-doped magnetic porous carbon was successfully prepared by a one-step, direct synthesis, simultaneous activation-graphitization and activation route. The as-prepared N-MPC material showed four advantages: ultrahigh surface area (~2148.42 m^2 g^{-1}), high pore volume (~1.26 cm^3 g^{-1}), homogeneous distribution of metallic Ni(0) and magnetic properties, resulting in superb adsorption performance and the reduction of Cr(VI) to Cr(III), and rapid separation from solution. The synthesized N-MPC is stable and environmentally friendly with an excellent removal capacity of ~1284.09 mg g^{-1} for MB. Moreover, the surface adsorbed Cr(VI) can be reduced into Cr(III) on the surface of N-MPC by metallic Ni(0). Its facile, scalable synthesis and unique structures demonstrate that this new N-MPC material can be potentially applied for its fast removal rate, high removal capacity, and magnetic separation in wastewater treatment. In addition, the ultrahigh surface area and large pore volume of N-MPC has great potential in many future applications, such as lithium ion batteries, supercapacitors, and in photocatalysis. More detailed application of the N-MPC will be carried out in our future research work.

Acknowledgements

The authors acknowledge the financial support from the Ministry of Science and Technology of China (2011CB933700), the National Natural Science Foundation of China (21225730, 91326202, 21207136 and 21272236), and Hefei Center for Physical Science and Technology (2012FXZY005).

Notes and references

1 X. L. Yu, S. R. Tong, M. F. Ge, J. C. Zuo, C. Y. Cao and W. G. Song, *J. Mater. Chem. A*, 2013, **1**, 959–965.
2 X. L. Yang, X. Y. Wang, Y. Q. Feng, G. Q. Zhang, T. S. Wang, W. G. Song, C. Y. Shu, L. Jiang and C. R. Wang, *J. Mater. Chem. A*, 2013, **1**, 473–477.
3 Y. X. Zhang, X. Y. Yu, Z. Jin, Y. Jia, W. H. Xu, T. Luo, B. J. Zhu, J. H. Liu and X. J. Huang, *J. Mater. Chem.*, 2011, **21**, 16550–16557.
4 S. W. Zhang, M. Y. Zeng, J. X. Li, J. Li, J. Z. Xu and X. K. Wang, *J. Mater. Chem. A*, 2014, **2**, 4391–4397.
5 S. W. Zhang, W. Q. Xu, M. Y. Zeng, J. Li, J. X. Li, J. Z. Xu and X. K. Wang, *J. Mater. Chem. A*, 2013, **1**, 11691–11697.
6 X.-Y. Yu, R.-X. Xu, C. Gao, T. Luo, Y. Jia, J. H. Liu and X. J. Huang, *ACS Appl. Mater. Interfaces*, 2012, **4**, 1954–1962.
7 R. Wang, S. H. Guan, A. Sato, X. Wang, Z. Wang, R. Yang, B. S. Hsiao and B. Chu, *J. Membr. Sci.*, 2013, **446**, 376–382.
8 X. Y. Yu, T. Luo, Y. Jia, Y. X. Zhang, J.-H. Liu and X. J. Huang, *J. Phys. Chem. C*, 2011, **115**, 22242–22250.
9 C. Y. Cao, J. Qu, F. Wei, H. Liu and W. G. Song, *ACS Appl. Mater. Interfaces*, 2012, **4**, 4283–4287.
10 X.-Y. Yu, T. Luo, Y. X. Zhang, Y. Jia, B.-J. Zhu, X. C. Fu, J. H. Liu and X.-J. Huang, *ACS Appl. Mater. Interfaces*, 2011, **3**, 2585–2593.
11 Z. Wei, R. Xing, X. Zhang, S. Liu, H. Yu and P. Li, *ACS Appl. Mater. Interfaces*, 2012, **5**, 598–604.
12 Y. Jia, X. Y. Yu, T. Luo, M. Y. Zhang, J. H. Liu and X. J. Huang, *Dalton Trans.*, 2013, **42**, 1921–1928.
13 X. K. Wang, C. L. Chen, W. P. Hu, A. P. Ding, D. Xu and X. Zhou, *Environ. Sci. Technol.*, 2005, **39**, 2856–2860.
14 C. H. Wu, *J. Hazard. Mater.*, 2007, **144**, 93–100.
15 K. Kadirvelu, M. Kavipriya, C. Karthika, M. Radhika, N. Vennilamani and S. Pattabhi, *Bioresour. Technol.*, 2003, **87**, 129–132.
16 G. X. Zhao, J. X. Li, X. M. Ren, C. L. Chen and X. K. Wang, *Environ. Sci. Technol.*, 2011, **45**, 10454–10462.
17 S. W. Zhang, M. Y. Zeng, W. Q. Xu, J. X. Li, J. Li, J. Z. Xu and X. K. Wang, *Dalton Trans.*, 2013, **42**, 7854–7858.
18 C. Gao, X. Y. Yu, T. Luo, Y. Jia, B. Sun, J. H. Liu and X. J. Huang, *J. Mater. Chem. A*, 2014, **2**, 2119–2128.
19 H. C. Gao, Y. M. Sun, J. J. Zhou, R. Xu and H. W. Duan, *ACS Appl. Mater. Interfaces*, 2013, **5**, 425–432.
20 M. C. Liu, C. L. Chen, J. Hu, X. L. Wu and X. K. Wang, *J. Phys. Chem. C*, 2011, **115**, 25234–25240.
21 H. M. Sun, L. Y. Cao and L. H. Lu, *Nano Res.*, 2011, **4**, 550–562.
22 Y. W. Zhu, S. Murali, M. D. Stoller, K. J. Ganesh, W. W. Cai, P. J. Ferreira, A. Pirkle, R. M. Wallace, K. A. Cychosz, M. Thommes, D. Su, E. A. Stach and R. S. Ruoff, *Science*, 2011, **332**, 1537–1541.
23 Y. Y. Li, Z. S. Li and P. K. Shen, *Adv. Mater.*, 2013, **25**, 2474–2480.
24 W. J. Liu, K. Tian, H. Jiang and H. Q. Yu, *Sci. Rep.*, 2013, **3**, 2419–2425.
25 C. H. Huang, R. A. Doong, D. Gu and D. Y. Zhao, *Carbon*, 2011, **49**, 3055–3064.
26 L. Sun, C. G. Tian, Y. Fu, Y. Yang, J. Yin, L. Wang and H. G. Fu, *Chem.–Eur. J.*, 2014, **20**, 564–574.
27 L. H. Liu, G. Zorn, D. G. Castner, R. Solanki, M. M. Lerner and M. D. Yan, *J. Mater. Chem.*, 2010, **20**, 5041–5046.
28 L. Sun, C. Tian, L. Wang, J. Zou, G. Mu and H. Fu, *J. Mater. Chem.*, 2011, **21**, 7232–7239.
29 L. Panchakarla, A. Govindaraj and C. Rao, *ACS Nano*, 2007, **1**, 494–500.
30 Z. H. Sheng, L. Shao, J.-J. Chen, W. J. Bao, F. B. Wang and X.-H. Xia, *ACS Nano*, 2011, **5**, 4350–4358.
31 J. Wu, D. Zhang, Y. Wang and B. Hou, *J. Power Sources*, 2013, **227**, 185–190.
32 A. M. Liu, K. Hidajat, S. Kawi and D. Y. Zhao, *Chem. Commun.*, 2000, 1145–1146.
33 Z. Liu, G. Zhang, Z. Lu, X. Jin, Z. Chang and X. Sun, *Nano Res.*, 2013, **6**, 293–301.
34 A. Fischer, M. Antonietti and A. Thomas, *Adv. Mater.*, 2007, **19**, 264–267.
35 A. Fischer, J. O. Müller, M. Antonietti and A. Thomas, *ACS Nano*, 2008, **2**, 2489–2496.
36 Z. Wen, X. Wang, S. Mao, Z. Bo, H. Kim, S. Cui, G. Lu, X. Feng and J. Chen, *Adv. Mater.*, 2012, **24**, 5610–5616.
37 Y. Hou, Z. Wen, S. Cui, X. Guo and J. Chen, *Adv. Mater.*, 2013, **25**, 6291–6297.
38 N. Wu, H. Wei and L. Zhang, *Environ. Sci. Technol.*, 2011, **46**, 419–425.
39 T. Karanfil and J. E. Kilduff, *Environ. Sci. Technol.*, 1999, **33**, 3217–3224.
40 L. Billon, V. Meric, A. Castetbon, J. Francois and J. Desbrieres, *J. Appl. Polym. Sci.*, 2006, **102**, 4637–4645.
41 W. E. Oliveira, A. S. Franca, L. S. Oliveira and S. D. Rocha, *J. Hazard. Mater.*, 2008, **152**, 1073–1081.
42 Y. Li, S. M. Zhu, Q. L. Liu, Z. X. Chen, J. J. Gu, C. L. Zhu, T. Lu, D. Zhang and J. Ma, *Water Res.*, 2013, **47**, 4188–4197.
43 M. Pérez-Candela, J. Martín-Martínez and R. Torregrosa-Maciá, *Water Res.*, 1995, **29**, 2174–2180.
44 C. Weng, J. Wang and C. Huang, *Water Sci. Technol.*, 1997, **35**, 55–62.
45 J. Hu, G. Chen and I. Lo, *Water Res.*, 2005, **39**, 4528–4536.
46 X. F. Sun, Y. Ma, X. W. Liu, S. G. Wang, B. Y. Gao and X. M. Li, *Water Res.*, 2010, **44**, 2517–2524.
47 D. Park, Y.-S. Yun and J. M. Park, *Chemosphere*, 2005, **60**, 1356–1364.
48 G. Walker and L. Weatherley, *Chem. Eng. J.*, 2001, **83**, 201–206.
49 J. Ma, F. Yu, L. Zhou, L. Jin, M. Yang, J. Luan, Y. Tang, H. Fan, Z. Yuan and J. Chen, *ACS Appl. Mater. Interfaces*, 2012, **4**, 5749–5760.
50 X. Zhuang, Y. Wan, C. Feng, Y. Shen and D. Zhao, *Chem. Mater.*, 2009, **21**, 706–716.
51 Y. Dong, H. Lin, Q. Jin, L. Li, D. Wang, D. Zhou and F. Qu, *J. Mater. Chem. A*, 2013, **1**, 7391–7398.